Journal Pre-proof

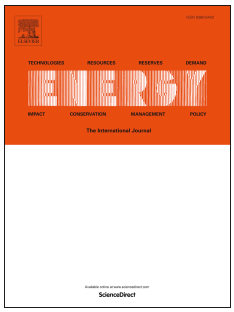

Hydration State Measurement in Polymer Electrolyte Fuel Cells from Correlated Neutron Imaging and Single-Point Impedance

Y. Wu, S. Zhou, J. Chen, B. Li, J. Li, W. Kockelmann, Y. Han, Q. Li, W. Chen, P.R. Shearing, D.J.L. Brett, T.S. Miller, R. Jervis

PII: S0360-5442(25)05407-6

DOI: https://doi.org/10.1016/j.energy.2025.139764

Reference: EGY 139764

To appear in: *Energy*

Received Date: 4 September 2025

Revised Date: 26 November 2025

Accepted Date: 21 December 2025

Please cite this article as: Wu Y, Zhou S, Chen J, Li B, Li J, Kockelmann W, Han Y, Li Q, Chen W, Shearing PR, Brett DJL, Miller TS, Jervis R, Hydration State Measurement in Polymer Electrolyte Fuel Cells from Correlated Neutron Imaging and Single-Point Impedance, *Energy*, https://doi.org/10.1016/j.energy.2025.139764.

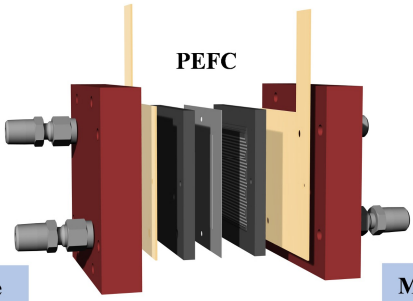

Single-frequency Impedance Phase Angle at 40 Hz

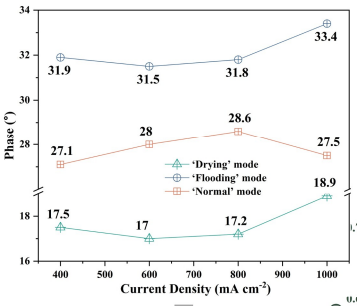

Measuring Water Mass from *Operando* Neutron Images

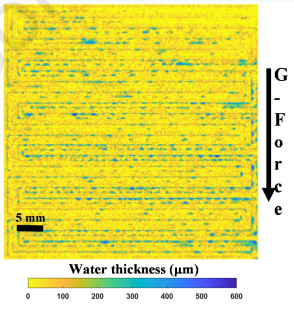

Evolution of Voltage, Water Mass, and Phase Angle

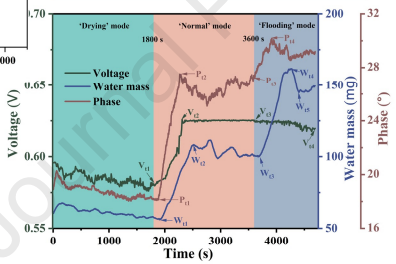

The Correlation Coefficient Matrix

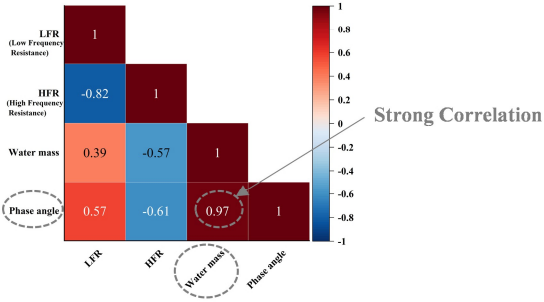

Hydration State Measurement in Polymer Electrolyte Fuel Cells from Correlated Neutron Imaging and Single-Point Impedance

Y. Wu, [a,b,c] S. Zhou, [b,*] J.Chen, [b] B. Li,[b] J. Li,[b] W. Kockelmann, [d] Y. Han,[a] Q. Li,[a] W. Chen,[a,c] P. R. Shearing,[e] D. J. L. Brett,[f] T. S. Miller,[b,g] R. Jervis [b,g,*]

[a]*School of Electrical Engineering, Southwest Jiaotong University, Chengdu, Sichuan Province 611756, China.*
[b]*Electrochemical Innovation Lab (EIL), Department of Chemical Engineering, University College London, London WC1E 7JE, United Kingdom.*
[c]*Sichuan Rongchuang New Energy Power System Co., Ltd, Chengdu, Sichuan Province 610511, China.*
[d]*Science and Technology Facilities Council (STFC), Rutherford Appleton Laboratory, ISIS Facility, Harwell OX11 0QX, United Kingdom.*
[e]*Engineering Science and ZERO Institute, Department of Engineering Science, University of Oxford, Parks Road, Oxford, Oxfordshire, OX1 3PJ, United Kingdom.*
[f]*Prosemino Limited, Unit 2, Paper Yard, Quebec Way, London SE16 7LG, UK.*
[g]*Advanced Propulsion Lab (APL), University College London, Marshgate, London, E20 2AE, UK.*

[*]Corresponding authors.
Email address: shangwei.zhou.20@ucl.ac.uk (S. Zhou), rhodri.jervis@ucl.ac.uk (R. Jervis).

Abstract

Effective water management remains a critical challenge for polymer electrolyte fuel cell (PEFC) durability and reliability, necessitating accurate real-time hydration state monitoring. Full-spectrum electrochemical impedance spectroscopy (EIS) struggles to balance diagnostic speed with accuracy, and the linkage between microscopic liquid water distribution and macroscopic EIS parameters remains inadequately resolved. This study introduces a novel method using the 40 Hz single-frequency impedance phase angle, integrated with *operando* neutron imaging, for non-invasive, rapid hydration state assessment in operating PEFCs. The methodology was validated across three operational modes (Drying, Normal, Flooding). While conventional parameters like high-frequency resistance (HFR) effectively identified membrane dehydration and low-frequency resistance (LFR) detected cathodic flooding, neutron imaging revealed that neither HFR nor LFR consistently correlated with total liquid water mass across all states. Specifically, LFR showed strong water mass correlation in Drying mode ($r = 0.98$) but declined significantly in Normal ($r = 0.76$) and Flooding ($r = 0.39$) modes. In contrast, the 40 Hz phase angle maintained strong positive correlations ($r \geqslant 0.89$) universally across all hydration states and operational regimes. Crucially, terminal voltage remained stable despite substantial hydration fluctuations during Normal mode operation (e.g., water mass: 98–111 mg; phase angle: 25.1°–27.5°),

underscoring its inadequacy for hydration detection. The phase angle also dynamically captured pore-blocking and channel-clearing events during Flooding mode, while voltage responses lagged behind mass transport limitations. These findings establish the 40 Hz impedance phase angle as a rapid, accurate, and robust indicator for real-time PEFC hydration assessment, enabling future advanced water management strategies.

Keywords: Polymer electrolyte fuel cells; Water management; Electrochemical impedance spectroscopy; Neutron imaging; Phase angle.

1. Introduction

Polymer electrolyte fuel cells (PEFCs) have become a leading clean energy technology in hydrogen systems due to their high energy conversion efficiency, low environmental impact and rapid startup capabilities [1, 2]. Effective water management is crucial for optimizing PEFC performance and durability [3, 4]. While adequate hydration ensures proton conductivity in the polymer electrolyte, excessive liquid water in gas diffusion electrodes (GDEs) and flow channels hinders reactant transport, reduces reaction kinetics and causes voltage fluctuations [5, 6]. Effective water management of PEFC is therefore critical for maintaining membrane hydration equilibrium while preventing flooding [7, 8]. Proper humidification of reactant gases maintains membrane hydration equilibrium, while excessive liquid water needs to be purged to prevent flooding-induced mass transport limitations, thereby sustaining optimal PEFC performance. This underscores the necessity for developing reliable methods to measure hydration states and enhance PEFC operational efficiency and lifespan.

Hydration state measurement in PEFCs employs two principal methodological approaches: non-imaging and imaging techniques. A common non-imaging technique is electrochemical impedance spectroscopy (EIS), which enables differentiation of polarization mechanisms through frequency-resolved impedance analysis, providing critical insights into multiphysics interactions, and the hydro state affects the various polarisation processes in PEFC. A comprehensive investigation of the water management's impact on commercial PEFC stacks through EIS by Moçotéguy et al revealed distinct capacitive and inductive loop formations under controlled humidity variations [9]. This work establishes a correlation between cathode dehydration and diminished ionomer proton conductivity,

with sub-45° phase angles in low-frequency inductive loops serving as quantitative dehydration markers. Comparative analysis of pristine and aged stack configurations further demonstrates progressive ionomer conductivity degradation. Subsequent research developed an advanced active humidification system incorporating fuzzy logic-controlled bypass valves to systematically regulate cathode inlet air relative humidity (30%-85% RH) [10]. Parallel implementation of an optimized EIS configuration demonstrated a 39% reduction in membrane resistance and a 23% decrease in charge transfer resistance with elevated humidity levels, culminating in 2.2% cell voltage improvement. These findings validate EIS as a powerful diagnostic technique for operational hydration monitoring and failure mode identification in PEFC systems.

EIS remains a powerful technique for water management analysis, though full-spectrum measurements face time constraints due to their duration (>5 minutes). To address this limitation, researchers have developed single-frequency impedance monitoring techniques that enable rapid assessment of water content states in PEFCs. An early fault diagnosis methodology for PEFCs was developed using the impedance phase angle as a rapid and non-invasive indicator of the internal hydration state [11]. This approach established specific phase angle thresholds, enabling the detection of drying conditions (phase angle $\leqslant 24°$) and flooding faults (phase angle $\geqslant 35°$) before any significant voltage degradation occurred, thereby facilitating proactive intervention. This diagnostic technique was advanced into a closed-loop water management strategy in subsequent research [12]. This strategy dynamically regulates the water content within the PEFC by intelligently coordinating the air stoichiometry for coarse, rapid adjustments and the stack temperature for fine-tuning, thereby achieving an optimal balance between system response speed and power loss. Recent advancements propose hybrid-frequency EIS methodologies that combine full-spectrum characteristic analysis with high-low frequency intersection features, achieving 95.56% diagnostic accuracy within 4 seconds through 3-kW platform validation under diverse operating conditions [13]. Our previous study proposed a novel AC voltage response and 1D CNN strategy for rapid PEFC diagnosis [14], bypassing EIS time-frequency conversion and steady-state limitations. While these approaches significantly reduce measurement

duration, further validation through direct visualization techniques is still required to establish the method's operational accuracy in practical applications.

Unlike the previously discussed non-imaging methods, imaging techniques offer the ability to ‘see inside’ and quantify water content, which primarily include synchrotron X-ray microscopy, optical visualization and neutron imaging. While synchrotron X-ray microscopy achieves high spatial resolution, its application remains limited to microscale PEFC configurations (<2 cm^2 active area) [15-17], restricting relevance to commercial-scale systems. Optical visualization techniques provide superior temporal resolution but suffer from inherent limitations, including the lack of quantitative water analysis and the requirement for cell structural modifications[18, 19]. Neutron imaging has emerged as a powerful technique, enabling quantitative liquid water mapping in operational full-scale PEFCs with original design (1–200 cm^2 active area) [20, 21]. This technique leverages neutrons' unique interaction properties: effective penetration of metallic bipolar plates combined with strong attenuation by hydrogen-rich water molecules. Such characteristics facilitate high spatial-temporal resolution analysis of water transport phenomena. Extensive applications include the investigation of water management fundamentals through parametric studies of cell design [22-25], compression parameters [26, 27], operational conditions [28, 29], material properties [30] and degradation mechanisms [31] on water distribution dynamics.

While neutron imaging provides quantitative water content analysis in PEFCs, its implementation faces technical constraints. The methodology inherently depends on centralized neutron sources with restricted accessibility, requiring specialized infrastructure that requires substantial operational costs. These limitations make real-time in situ neutron imaging for dynamic water management scenarios impractical. Consequently, complementary diagnostic approaches that balance spatial resolution with practical implementation feasibility are required. Establishing correlations between macroscopic impedance parameters (e.g., phase angles) and microscopic water distribution is thus imperative. Our previous study integrates synchronous EIS and neutron imaging to correlate water content in operational PEFCs [32]. Machine learning models bridge EIS data with neutron-derived water distribution, enabling water estimation via cost-effective EIS. However, the full-spectrum EIS data were still required in this approach, resulting in time constraints. Furthermore, only two PEFC water management states were

employed by alternating dry/humid air supply, neglecting the impacts of hydrogen humidity, cell temperature, and gas flow rate [33].

The current study employs neutron radiography to quantify spatial water distribution patterns in operational PEFCs under three distinct hydration states: Drying, Normal, and Flooding. A quantitative correlation is established between the macroscopic impedance response, specifically the phase angle at 40 Hz, and the microscale liquid water mass dynamics, thereby enabling a calibration that eliminates the reliance on costly neutron imaging for subsequent diagnosis. By cross-validating EIS-derived parameters with direct water data, this method provides a robust, non-invasive tool for real-time water management, which holds significant potential for advancing fault diagnosis strategies in practical PEFC systems where complex and expensive imaging setups are infeasible.

2. Experimental setup

2.1. PEFC design

The PEFC used in this study was fabricated in-house, employing a membrane electrode assembly (MEA) with an active area of 25 cm^2. The MEA was prepared by hot-pressing GDEs (HyPlat, South Africa) featuring a platinum catalyst loading of 0.4 mg Pt cm^{-2} and a Gore Select membrane (GORE M765.08, USA) at 150°C for 3 minutes under a compression force of 1000 psi. Prior to formal experimental testing, the activation of the hot-pressed MEA was performed using potentiostatic operation mode (0.6 V, 2h) [34]. This process promotes membrane hydration through water generated by electrochemical reactions and water vapor provided by the humidification at the gas inlets. The activation was carried out at an operating temperature of 60 °C, with cathode and anode stoichiometric ratios set at 3 and 2, respectively, and the relative humidity of the inlet gases maintained at 70%. Additional components included graphite bipolar plates with double-serpentine flow fields (for both sides), anodised aluminium endplates and gold-coated current collectors. The flow-field plates were made of 2 mm thick graphite and designed with a dual-channel serpentine layout, each channel and rib measuring about 1 mm wide and 1 mm deep. To maintain even temperature distribution and avoid vapor condensation or localized overheating, Kapton flexible heaters were mounted on both sides of the endplates. The exploded view of the PEFC assembly is shown in supplementary materials (Fig. S1).

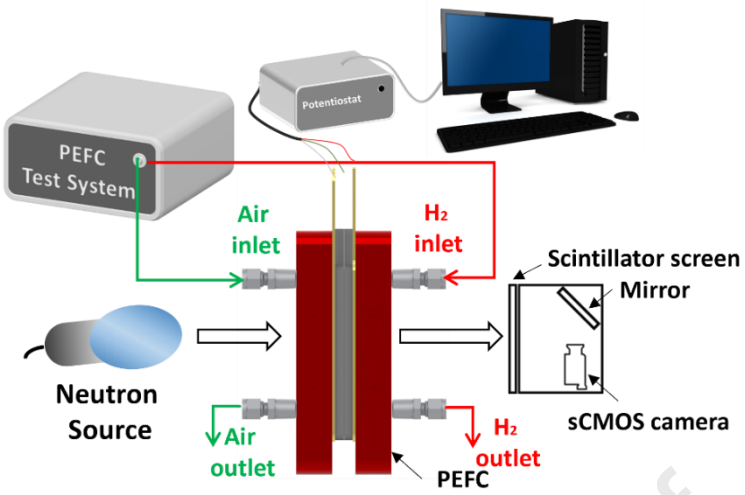

Fig. 1. Simplified schematic of the experimental setup.

2.2. Electrochemical Test Process

Polarization curve measurements were conducted using a Scribner 850e fuel cell test station (Scribner Associates, USA). The current density was increased from 0 to 1400 mA cm^{-2} in 200 mA cm^{-2} incremental steps to cover the activation, Ohmic and mass transport processes, with a termination criterion of cell voltage dropping below 0.5 V. Each current step maintained a 300-second stabilization duration to ensure steady-state equilibrium and mitigate transient electrochemical responses. The test station provided integrated control of operational parameters, including cell voltage monitoring, load and relative humidity (RH) control and thermal regulation.

To investigate operational impacts on water management of PEFC, three distinct operational modes - Normal, Drying, and Flooding were employed (Table 1). In Normal mode, baseline operation used H_2/air stoichiometric ratios of 2/3 with balanced humidification (70% RH at anode and cathode) and cell temperature at 60°C. Drying mode was designed through reduced humidification (40% RH) combined with elevated stoichiometric ratios (H_2:2.5, air:3.5) and increased cell temperature (65°C) to accelerate membrane dehydration via enhanced water extraction. Flooding conditions employed saturated reactant streams (100% RH) at 50°C with decreased stoichiometric ratios (H_2:2, air:2.5), reducing liquid water drainage capacity to induce flooding in PEFC.

Electrochemical impedance spectroscopy (EIS) was performed using a Gamry Reference 3000 potentiostat coupled with the Scribner 850e test system. Measurements were conducted at current

densities of 400, 600, 800 and 1000 mA cm^{-2} in galvanostatic mode (5% of DC current, 0.1 Hz to 10 kHz frequency range, 10 points per decade). The Nyquist plots were analyzed via equivalent circuit modelling (introduced in [24]) to decouple contributions from ohmic resistance (high frequency resistance, HFR), charge transfer resistance (mid-frequency semicircle), and mass transport resistance (low frequency resistance, LFR). A 10-minute current-stabilization protocol was implemented preceding each EIS measurement.

Table 1-Different water management mode used in the experiments.

Mode / Parameters	'Drying'	'Flooding'	'Normal'
Inlet RH/%	40	100	70
Cell temperature/ ℃	65	50	60
Stoichiometric flow ratio of H2/Air	2.5/3.5	2/2.5	2/3

2.3. Neutron imaging

Neutron imaging experiments were performed at the IMAT beamline (ISIS Neutron and Muon Source, Rutherford Appleton Laboratory, UK) [35]. The IMAT beamline used a collimated cold neutron beam (L/D ratio = 348) with a 98 × 98 mm^2 field of view and 96 μm pixel resolution. Neutron flux conversion employed a ZnS/LiF:Cu scintillator (0.1 mm thickness, Tritec Systems) coupled to an ANDOR IKON-L CCD camera, achieving time-resolved radiographs (2048 × 2048 pixels) at 30-second exposure intervals. The PEFC was oriented through-plane relative to the neutron beam path, ensuring the MEA plane was perpendicular to the neutron beam path for *operando* radiography. Neutron imaging experiments were synchronously conducted during both polarization curve testing and EIS measurements. The image setup provided an effective spatial resolution of 115 μm for tracking water mapping during steady-state operation. Raw neutron transmission intensity distributions obtained from the neutron imaging experiments were processed using ImageJ to quantify spatially resolved liquid water content:

(a) Image pre-processing (refer to '1' and '2' in Fig. 2): All recorded operational images, background images (acquired under dry conditions), and dark-field images (captured without neutron beam exposure) were subjected to median filtering to remove outlier noise. Subsequently, the pre-

processed background and dark-field images were averaged using a median stacking algorithm to enhance signal-to-noise ratios.

(b) Dark-field subtraction (refer to '3' in Fig. 2): Each filtered operational image was subtracted by the median-averaged dark-field image to eliminate detector-induced baseline artifacts.

(c) Dry image normalization (refer to '4' in Fig. 2): The median-averaged dry image was similarly subtracted by the processed dark-field image to isolate the neutron attenuation signal attributable solely to the PEFC components.

(d) Intensity normalization (refer to '3/4' in Fig. 2): The results from Steps (b) and (c) were divided pixel-wise in ImageJ, followed by grayscale normalization to produce images with intensity values scaled between 0 (full attenuation) and 1 (no attenuation).

(e) Liquid water thickness Conversion: The normalized grayscale images were transformed into liquid water thickness maps using the Beer-Lambert law [36].

(f) The averaged water mass of the PEFC under galvanostatic operation was quantified through spatial integration of pixel intensity-derived water thickness maps across the active area, using time-averaged neutron radiographs.

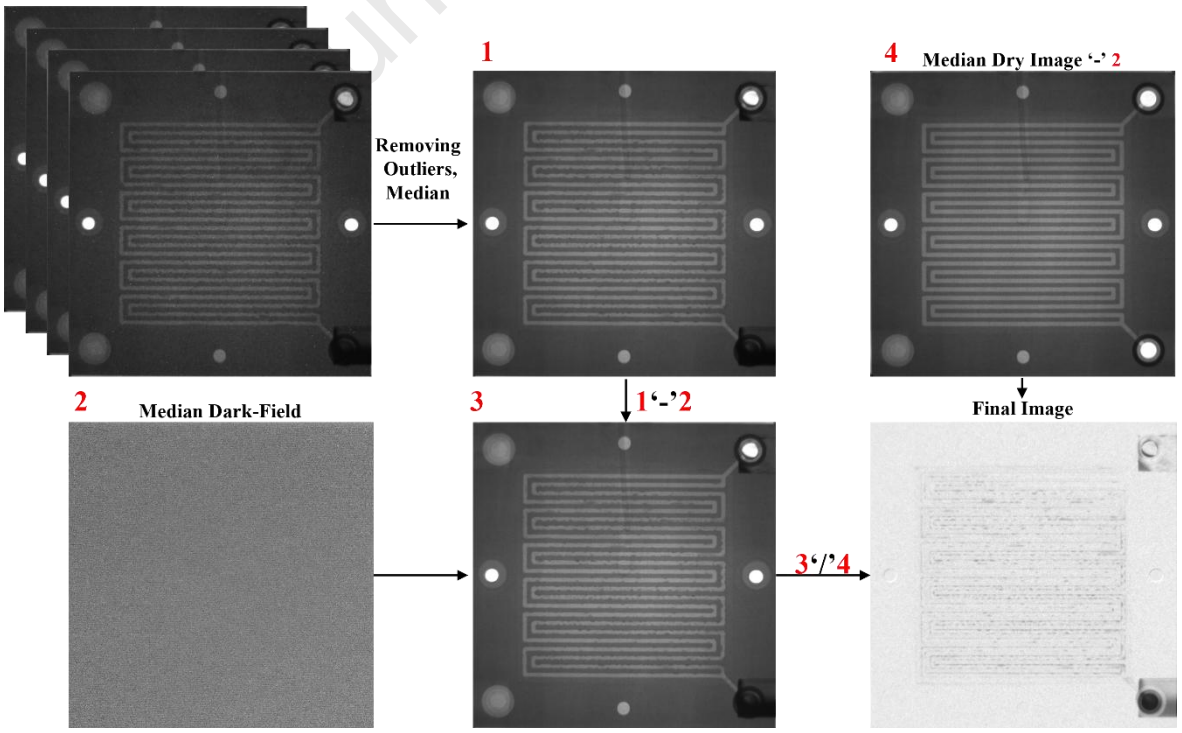

Fig. 2. Neutron images processing steps: (a) Image pre-processing (refer to '1' and '2'); (b) Dark-field subtraction (refer to '3'); (c) Dry image normalization (refer to '4'); (d) Intensity normalization (refer to '3/4'); (e) Final image.

3. Results and discussion

3.1 Electrochemical Performance

Fig. 3 illustrates the polarization curves and power density profiles of a PEFC under three operational modes. The PEFC exhibited comparable open-circuit voltage (OCV) values in three operational modes. At 200 mA cm^{-2} current density, the 'Flooding' mode displayed slightly higher performance (0.766 V) compared to 'Normal' (0.742 V) and 'Drying' mode (0.749 V). The superior performance of 'Flooding' mode could be due to elevated reactant humidity (100% RH), which improved membrane proton conductivity [37], without causing significant issues associated with flooding, as expected at this low current density. At 400 mA cm^{-2} current density, Ohmic polarization became progressively dominant. The Drying mode exhibited a lower output voltage (0.685 V) compared to Normal (0.691 V) and Flooding (0.766 V) modes, likely indicating incipient membrane dehydration that critically reduced proton conductivity and degraded performance [38]. The sustained superiority of Flooding mode over Normal mode at this stage suggests minimal concentration polarization effects. The performance difference between Flooding (0.621 V) and Normal (0.623 V) modes narrows at 800 mA cm^{-2}, contrasted with the widening disparity between Normal and Drying (0.586 V) modes. The Flooding mode's lower cell temperature reduced water saturation vapor pressure [39], coupled with lower stoichiometric flow ratios and elevated inlet relative humidity, concurrently exacerbated liquid water accumulation, ultimately degrading cell performance. On the other hand, the Drying mode likely experienced critical membrane dehydration under this current density, where electrochemically generated water failed to counteract the combined thermal and convective (higher stoichiometric flow ratio) dehydration effects. This imbalance elevated Ohmic polarization, ultimately causing severe performance deterioration. The polarization curves for the Drying and Flooding modes were tested up to 1000 mA cm^{-2} and 1200 mA cm^{-2}, respectively. Tests were terminated when output voltages in both modes fell below 0.5 V beyond these current densities. In contrast, the Normal mode demonstrated

more stable performance, maintaining an output voltage of 0.514 V at 1400 mA cm^{-2} without significant mass transport polarization, suggesting the absence of flooding failure at such high current density. Furthermore, the Normal mode achieved a power density of 589 mW cm^{-2} at 1000 mA cm^{-2} (the maximum current density among three modes), surpassing the Drying and Flooding modes by 9.5% and 2.1%, respectively.

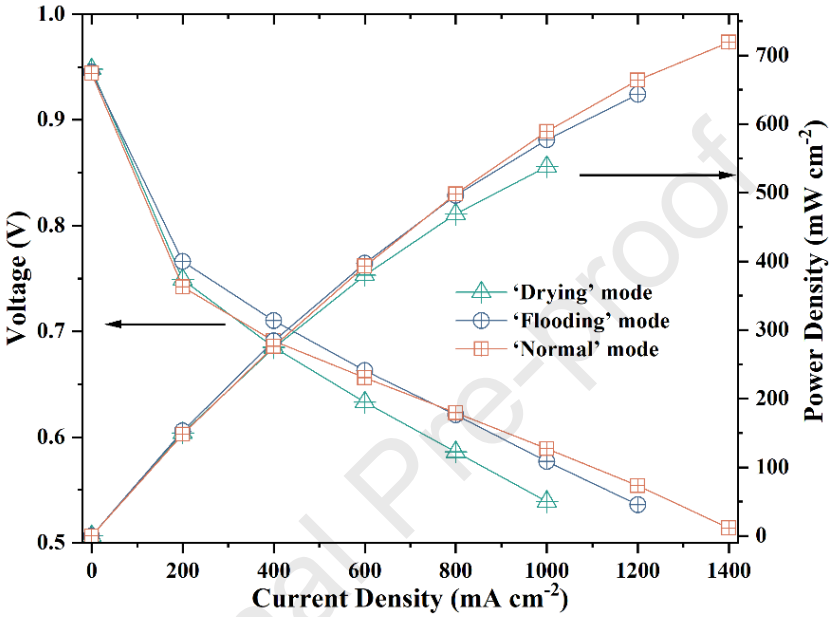

Fig. 3. Polarization curves for PEFCs at different operational modes.

3.2 Nyquist Plots Based on Electrochemical Impedance Spectroscopy

While polarization curve data enables comparative analysis of output performance disparities among three operating modes, it fails to elucidate the underlying mechanisms. EIS measurements were conducted under current densities of 400, 600, 800, and 1000 mA cm^{-2} for all three modes to address this limitation. A comparative analysis was conducted through Nyquist plots (as seen in Fig. 4), which revealed distinct impedance characteristics corresponding to each operational condition. Each subplot (a–d) displays experimental data (symbols) and fitted curves (lines). The fitting results exhibit strong agreement with the EIS experimental data.

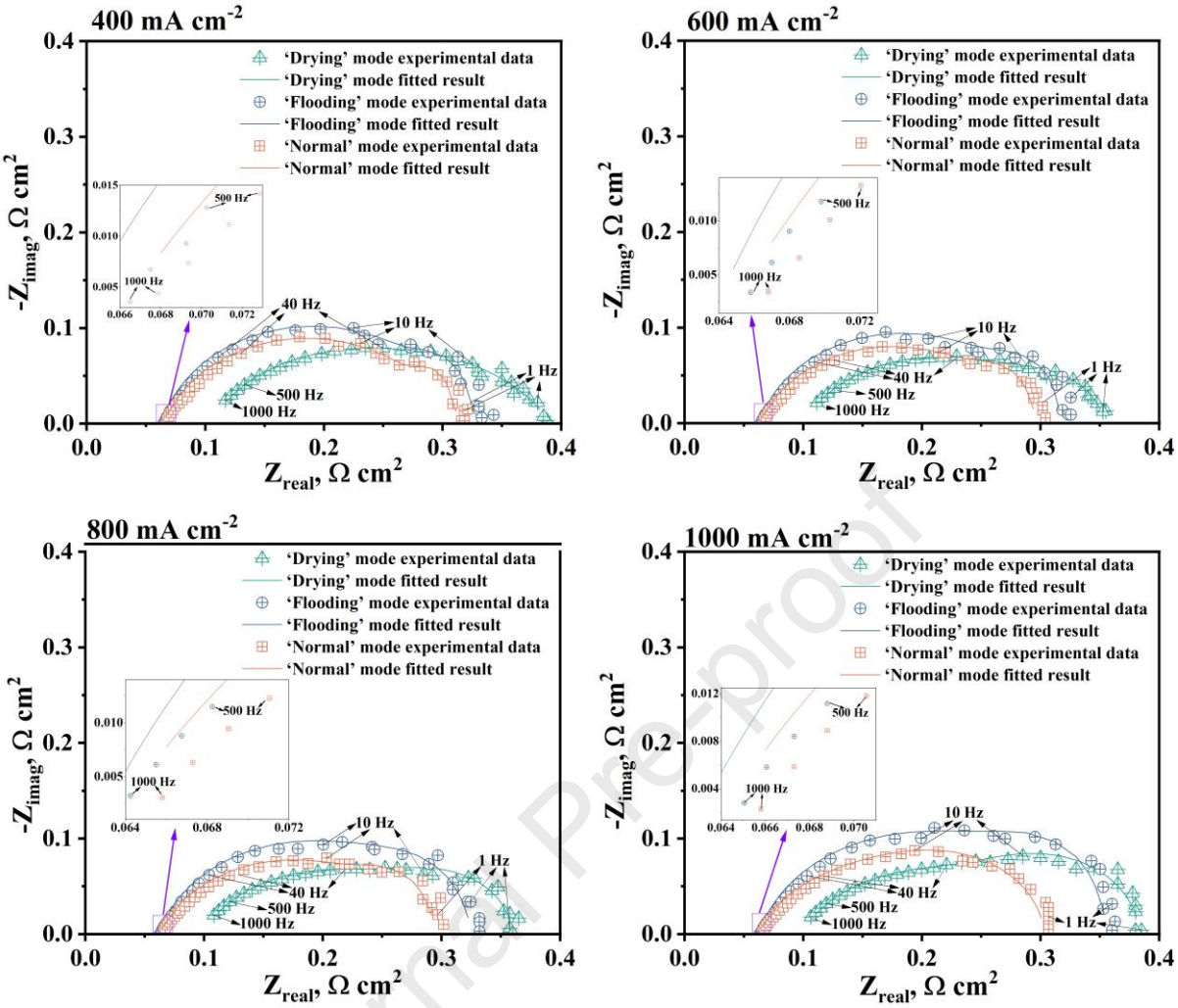

Fig. 4. Nyquist plots of the PEFC impedance spectroscopy at different current densities (a) 400 mA cm^{-2}; (b) 600 mA cm^{-2}; (a) 800 mA cm^{-2}; (d) 1000 mA cm^{-2}.

The intersection of the Nyquist plot with the real axis (high-frequency intercept) for Drying mode was significantly larger than those for Flooding mode and Normal mode across all current densities. This arises from membrane dehydration, which reduces proton conductivity and disrupts catalyst-layer hydration, amplifying activation polarization [40, 41]. Additionally, the semicircle diameter in the medium-frequency region of the Nyquist plot is significantly greater in Flooding mode than in both Drying mode and Normal mode across all current densities, indicating hindered electrode kinetics in Flooding mode. This is likely attributable to the lowest PEFC temperature (50°C) in this operating mode; additionally, the distance between the two real-axis intercepts of the Nyquist curve in Flooding mode is substantially larger than in Normal mode. Suggesting mass transport limitations in Flooding mode, which is due to excessive liquid water accumulation in GDEs, blocking gas diffusion [42].

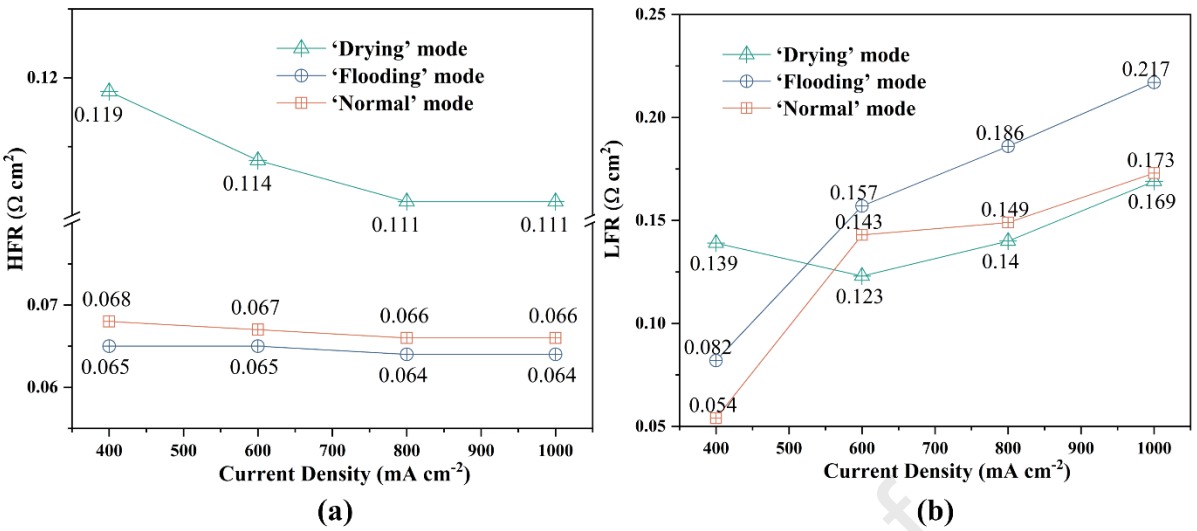

Fig. 5 Change in (a) high-frequency resistance (HFR) and low-frequency resistance (LFR) with respect to current density for PEFC at different operational modes.

The Nyquist plots were subsequently analyzed via equivalent circuit modelling to decouple contributions from HFR and LFR of the PEFC at current densities of 400-1000 mA cm^{-2}, as seen in Fig. 5. The HFR and LFR trends reveal distinct water management challenges across operational modes. Drying mode consistently demonstrates the highest HFR, exceeding Normal and Flooding modes, which has been discussed. Besides, all modes display HFR reduction with increasing current density, which is attributed to the self-humidification effect caused by the water produced during operation, and aligns with previous studies [43, 44]. Drying mode shows a 6.7% decline from 0.119 to 0.111 Ω cm^2, attributed to marginal hydration improvement from cathode-generated water. Conversely, HFR in Normal and Flooding modes exhibits a markedly smaller reduction magnitude with increasing current density. Beyond 800 mA cm^{-2}, HFR stabilization occurs at both Flooding and Normal mode, indicating membrane hydration saturation through electrochemically generated water. This plateau confirms sufficient water retention under two operational modes.

The LFR evolution across operating modes reveals mass transport mechanisms, as seen in Fig. 5 (b). In Drying mode, LFR initially decreases from 0.139 to 0.123 Ω cm^2 when current density increases from 400 to 600 mA cm^{-2} as electrochemical water generation temporarily alleviates membrane dehydration, but the subsequent higher LFR emerges at higher current densities [45]. Normal and Flooding modes exhibit higher LFR with increasing current density. Both modes exhibit a dramatic increase in LFR

between 400-600 mA cm^{-2} due to liquid water accumulation. Above 600 mA cm^{-2}, the Normal mode demonstrates a relatively smaller magnitude of LFR increase with current density compared to Flooding mode, indicating mitigated mass transport limitations as drainage mechanisms partially offset flooding. The disparity in LFR between Flooding and Normal modes escalates from 0.014 Ω cm^2 at 600 mA cm^{-2} to 0.044 Ω cm^2 at 1000 mA cm^{-2}, primarily attributed to Flooding mode's constrained gas flow velocity compounded by excessive water vapor influx. This causes inadequate liquid water removal at high current densities, inducing severe mass transport limitations that dominate performance decrease.

The divergent trends of HFR and LFR with current density are due to competing mechanisms: elevated current densities enhance water generation via electrochemical reactions, typically reducing HFR (under insufficient membrane hydration conditions), while inefficient water removal causes blockage in flow channels/GDL pores [46], impeding gas transport to reactive interfaces and amplifying LFR. This demonstrates that HFR could effectively distinguish Drying mode from Normal mode, while LFR reliably differentiates Flooding mode from Normal mode. However, in practical applications, the dynamic nature of PEFC systems introduces significant noise interference in measurements below 1 Hz [47]. Subsequently, the frequency-domain features embedded in Bode plots of impedance spectra to develop a hydration state identification methodology that balances accuracy with real-time applicability.

3.3 Bode Plots Based on Comprehensive Electrochemical Impedance Spectroscopy

Previous research has shown a correlation between impedance phase values near the phase angle peak and the hydration state in PEFCs [9, 12]. Therefore, it is imperative to determine the frequency band ranges containing peak phase angles in Bode plots under distinct operating modes. The impedance phase angles measured at optimal frequency points within these bands will serve as the basis for the hydration state identification of PEFC. Bode magnitude plots of the PEFC at different operational modes are provided in the supplementary materials (Fig. S2).

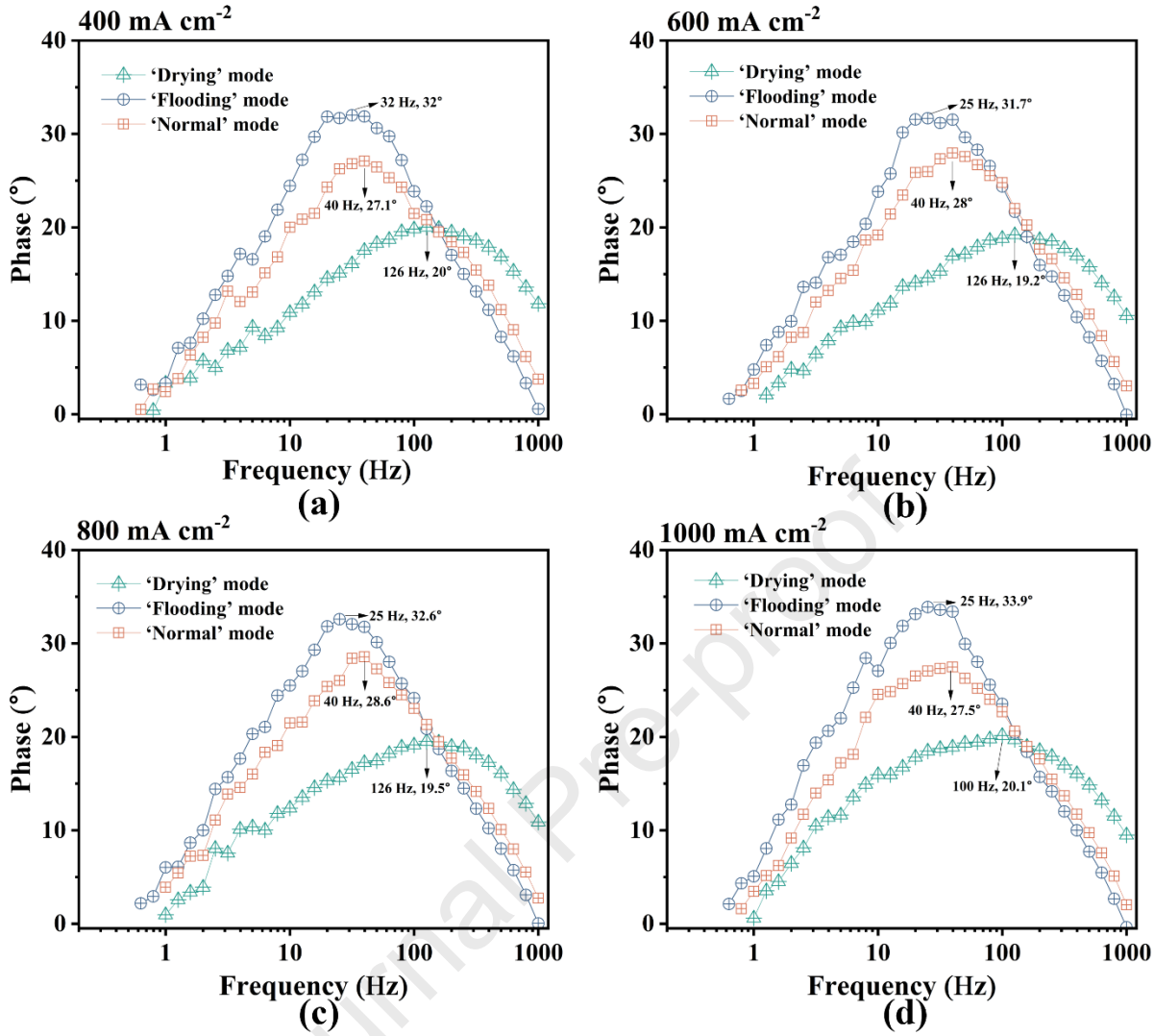

Fig. 6. Bode phase plots of the PEFC at different operational modes (a) 400 mA cm^{-2}; (b) 600 mA cm^{-2}; (c) 800 mA cm^{-2}; (d) 1000 mA cm^{-2}.

Fig. 6 presents Bode phase plots of experimental EIS data for PEFC under different modes at current densities of 400-1000 mA cm^{-2}. Each subplot includes arrows marking peak phase angles for each mode. The impedance phase values within the medium frequency band (10-80 Hz) exhibit significant discriminability among Normal, Flooding and Drying mode: Drying mode consistently shows the minimum phase angles, while Flooding mode displays the maximum phase angles, which aligns with [12, 48]. Consequently, impedance phase values within the frequency band corresponding to peak phase angles can serve as the indicator for identifying the hydration state of PEFCs.

To select optimal measurement frequency, ten frequency points within the 10-80 Hz band exhibiting significant mode discriminability in Fig. 6 were analyzed. $\Delta\theta_i$ denotes the minimum phase difference

between Flooding and Normal modes across frequencies in Bode phase plots, and $\Delta\theta_2$ denotes the minimum phase difference between Normal and Drying modes. These $\Delta\theta_1$ and $\Delta\theta_2$ values corresponding to each frequency point are summarized in Table 2.

Table 2-Minimum phase differences between Normal and Flooding modes, Normal and Drying modes in Bode phase plots.

f/Hz	10	13	16	20	25	32	40	50	63	80
$\Delta\theta_1$/°	2.5	4.3	5.5	5.7	5.4	3.6	3.2	2.1	1.6	1
$\Delta\theta_2$/°	8.1	8	8.4	8.7	8.6	8.6	8.6	6.9	5.7	4.2

As demonstrated by $\Delta\theta_1$ in Table 2, the frequency band exhibiting optimal flooding identification is within the 13-40 Hz band, while $\Delta\theta_2$ analysis reveals the Drying mode achieves maximum discriminability within an alomost identical 10-40 Hz band. Consequently, the overlapping 13-40 Hz frequency band, as the intersection of both ranges, is identified as the optimal frequency range for differentiating Normal, Flooding and Drying modes. Within this band, phase differences between Flooding and Normal states measure 3.2°-5.7°, while Drying vs. Normal modes exhibit 8°-8.7° phase disparities. Impedance phase measurements at any frequency within this range enable reliable identification of both flooding and drying conditions in PEFCs. The selection of elevated impedance measurement frequencies inherently reduces perturbation durations, which minimizes external interference and enhances measurement stability [47]. Furthermore, 40 Hz was selected as the optimal measurement frequency (upper limit of the 13–40 Hz spectrum) due to its diagnostic efficacy parity with alternative frequencies and significantly reduced measurement duration (25 ms per data point vs 100 ms for 10 Hz), thereby enabling rapid data acquisition and eliminating prolonged steady-state stabilization requirements for fuel cell systems. Phase angle measurements at this frequency exhibited robust discriminative capability, allowing precise differentiation among PEFC operational modes.

Fig. 7 presents 40 Hz phase angle values derived from Bode plots of PEFCs under Drying, Normal, and Flooding modes across current densities (400-1000 mA cm^{-2}). The drying mode consistently exhibits the lowest phase angles, whereas flooding mode demonstrates the highest values. Both modes display the same phase angle evolution trend with increasing current density: an initial decline from 400 to 600 mA cm^{-2}, followed by a progressive rise at higher currents (> 600 mA cm^{-2}). This behavior could

possibly be due to competing water management mechanisms. The initial reduction (400-600 mA cm^{-2}) stems from accelerated liquid water removal due to elevated reactant gas flow velocities under fixed stoichiometric control. However, beyond 600 mA cm^{-2}, higher electrochemical water production outweighs convective drainage enhancements, causing net water accumulation that elevates phase angles. In Normal mode, phase angles increase progressively from 400 to 800 mA cm^{-2}, reflecting optimized hydration from balanced water generation and removal. The subsequent 1.1° decrease in the phase angle at 1000 mA cm^{-2} results from the gas flow's removal capacity overwhelming accelerated electrochemical water generation [49].

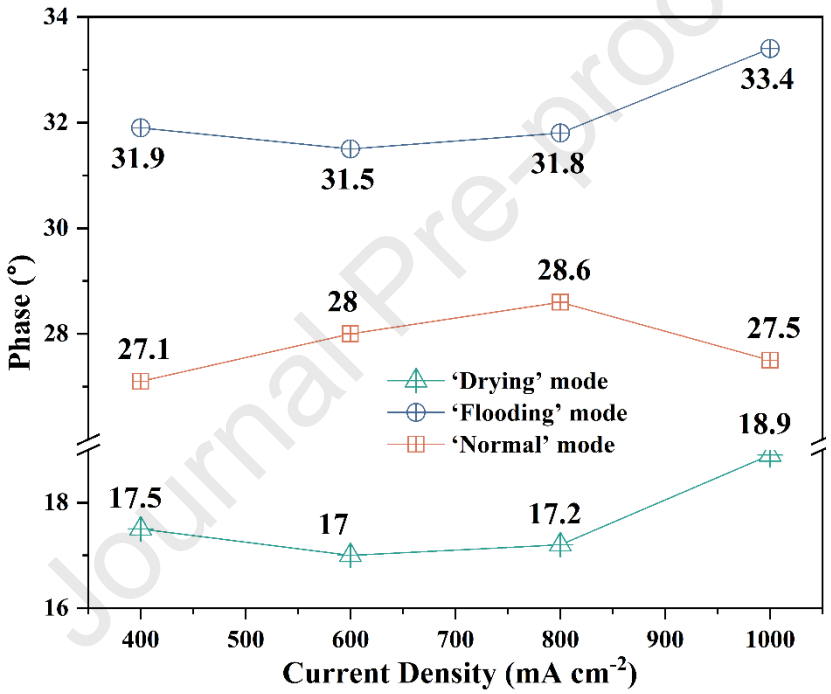

Fig. 7 Change in phase angle of PEFC with respect to current density at different water management modes.

3.4 Neutron Imaging

Comparative analysis of Fig. 5 and Fig. 7 demonstrates divergent trends in HFR, LFR and phase angle across operational modes with increasing current density. To establish diagnostic parameter validity for hydration state quantification, validation against neutron imaging experimental results remains essential. Fig. 8 compares the averaged water distribution of PEFCs under different water management modes during galvanostatic operation at 800 mA cm^{-2}. Neutron imaging data for other current densities (400, 600, and 1000 mA cm^{-2}) are provided in the supplementary materials (Fig. S3-5). Fig. 8 demonstrates

distinct liquid water distribution patterns across modes: In Drying mode, no large water clusters along flow channels are observed, but rather dispersed droplets (as seen in the magnified cut out of Fig. 8 (a)) predominantly localized within the MEA regions. In Normal mode, prominent liquid water clusters are distributed along flow channels within the mid-lower cell regions, attributable to gravitational effects and the downward flow direction of reactant gases [43]. While no bulk water accumulation occurs in the mid-upper regions, thin liquid water films persist along gas channel walls (as seen in the magnified cutout of Fig. 8 (b)), likely sustained by capillary forces and residual condensation. Under Flooding mode, continuous liquid water columns extend throughout the entire active area, with both flow channels exhibiting persistent liquid water accumulation from inlet to outlet (as seen in the magnified cutout of Fig. 8 (c)) [22, 23]. This spatial distribution pattern demonstrates significantly higher internal water content compared to the Normal mode, primarily attributed to insufficient reactant gas velocity and compromised water expulsion capacity.

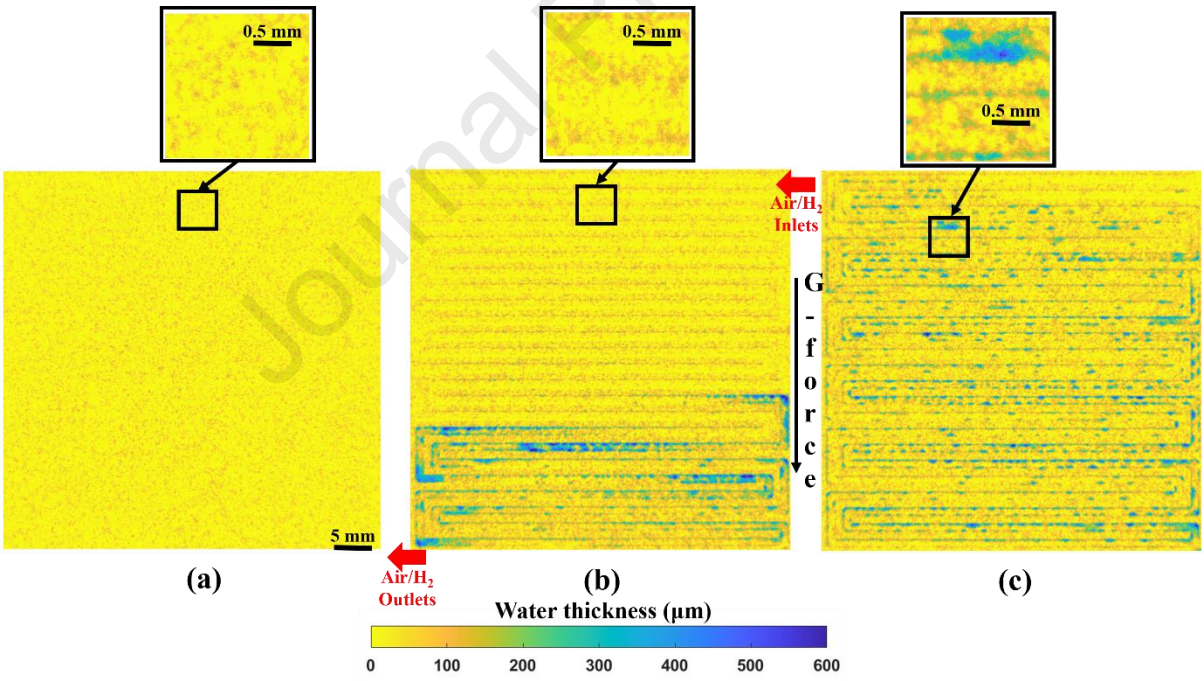

Fig. 8 Comparison of the averaged water distribution of PEFCs during galvanostatic operation at 800 mA cm^{-2} at different operational modes: (a) Drying, (b) Normal and (c) Flooding mode.

Figure 9 illustrates the change in the averaged liquid water mass of the PEFC with respect to current density under different operational modes. The quantification methodology for internal liquid water mass is detailed in Section 2.3. As shown in Figure 9, both Drying and Flooding modes exhibit similar

biphasic responses: a decrease in water mass occurs as current density increases from 400 to 600 mA cm^{-2}, followed by progressive increases at higher currents. This reversal arises when enhanced water removal rates from elevated gas flow velocities (400-600 mA cm^{-2}) become insufficient to offset intensified electrochemical water production (>600 mA cm^{-2}). In the Normal mode, the liquid water content increased with current density at low-to-medium ranges (400-800 mA cm^{-2}), although a 13% reduction occurred at 1000 mA cm^{-2}. This indicates that the enhanced gas flow rate at high current densities resulted in water removal surpassing the rate of water production [49].

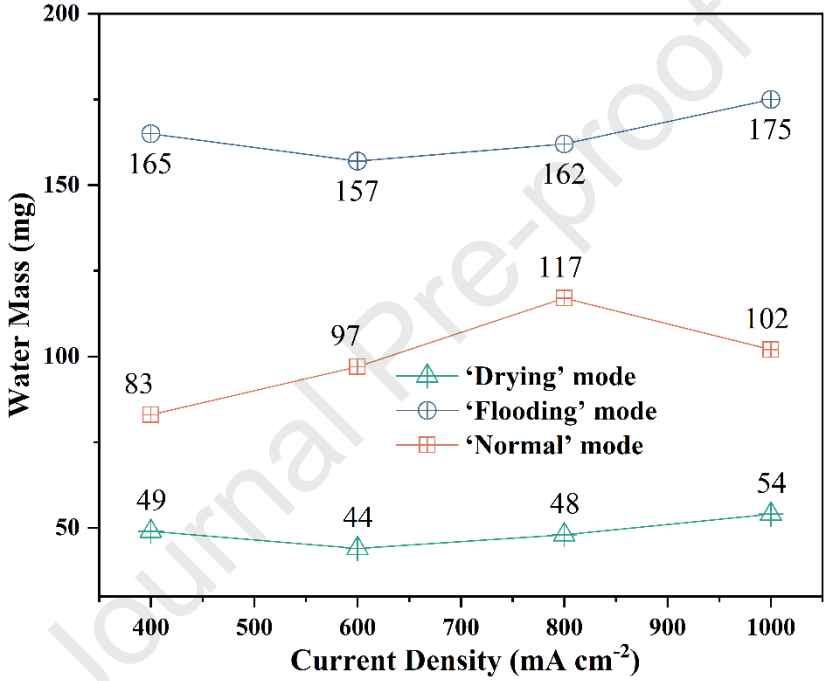

Fig. 9 Change in the averaged water mass of PEFC with respect to current density at different operational modes.

3.5 Correlation among LFR, HFR, phase angle and water mass

Correlation coefficient matrices [50] were computed to investigate relationships among LFR, HFR, 40 Hz phase angle, and liquid water mass, as depicted in Fig. 10. In Drying mode, HFR exhibits weak negative correlations with water mass (r=-0.26) and phase angle (r=-0.32), consistent with membrane dehydration simultaneously elevating bulk ionic resistance and impairing proton conductivity. Normal mode reveals significant LFR-HFR anticorrelation (r=-0.92), attributable to liquid water accumulation impeding gas diffusion (elevating LFR) while enhancing membrane hydration (reducing HFR). Phase

angle maintains strong positive correlation with water mass (r=0.89) in Normal mode. Flooding mode further demonstrates phase angle's diagnostic superiority, showing maximal correlation with water mass (r=0.97). Critically, while LFR exhibited significant positive correlations with water mass (r=0.98) under Drying mode, their correlation coefficient markedly declined in Normal (r=0.76) and Flooding modes (r=0.39); conversely, phase angle consistently retains strong positive correlations with water mass (r⩾0.89) across all operational regimes, thereby validating its efficacy as a robust hydration-state indicator for PEFCs.

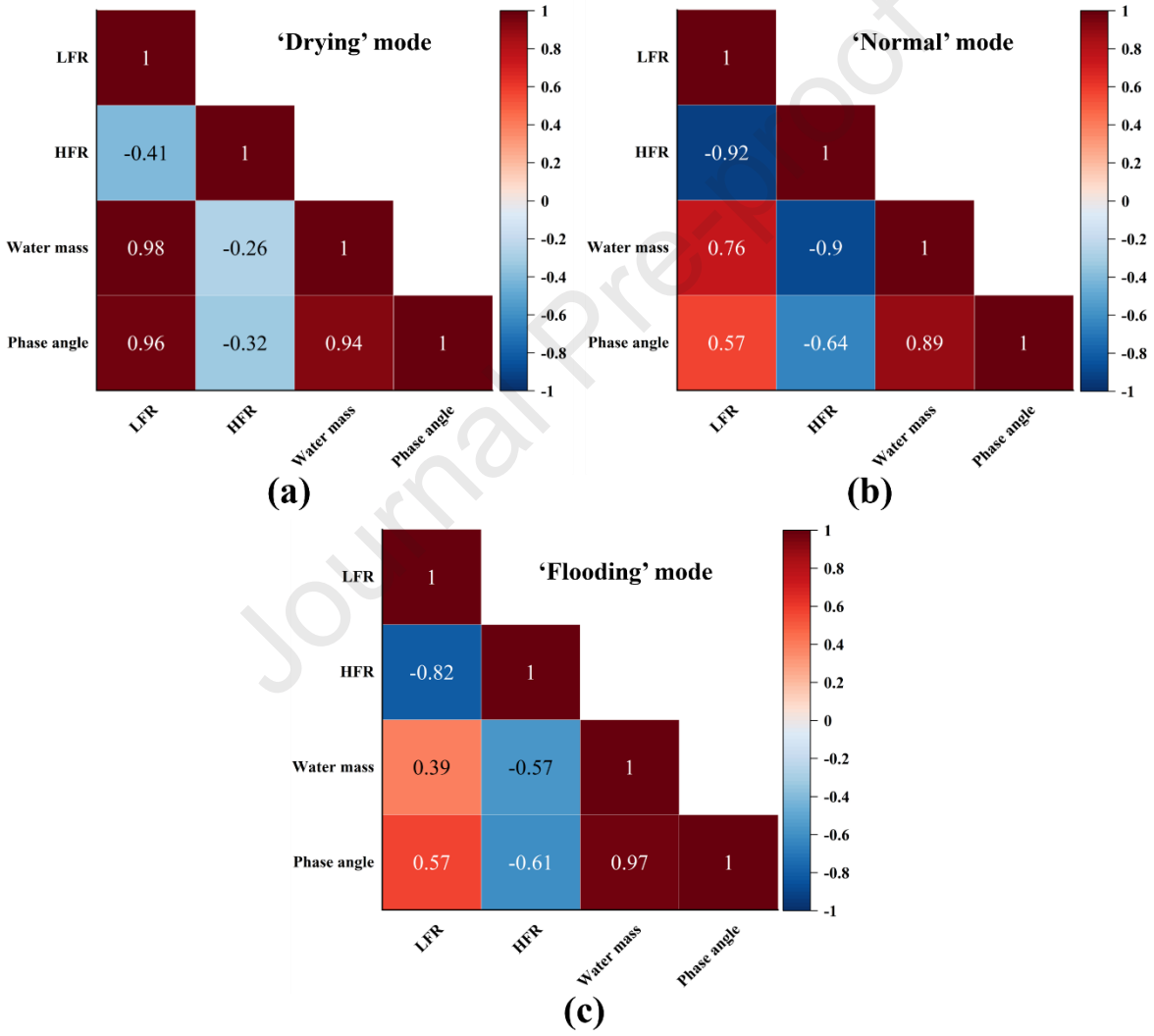

Fig. 10 The correlation coeffcient matrix between LFR, HFR, water mass and phase angle at different operational modes: (a) Drying, (b) Normal and (c) Flooding mode.

During operation, deviations from normal hydration ranges (toward drying/flooding) accelerate degradation of polymer electrolyte and catalyst layers despite minimal voltage decay, ultimately

compromising durability [9]. Consequently, water management systems capable of maintaining hydration within optimal thresholds could significantly enhance PEFC longevity [51]. Figure 11 shows the evolution of voltage (green circle, left axis), liquid water mass (blue triangle, right axis), and 40 Hz phase angle (brown square, secondary right axis) in a PEFC during galvanostatic operation at 800 mA cm^{-2}. This current density was selected since it exhibits a relatively small liquid water mass difference between Flooding mode and Normal mode (as seen in Fig. 9), thereby providing a scenario for validating the efficacy of the 40 Hz phase angle as an indicator of hydration state in PEFCs.

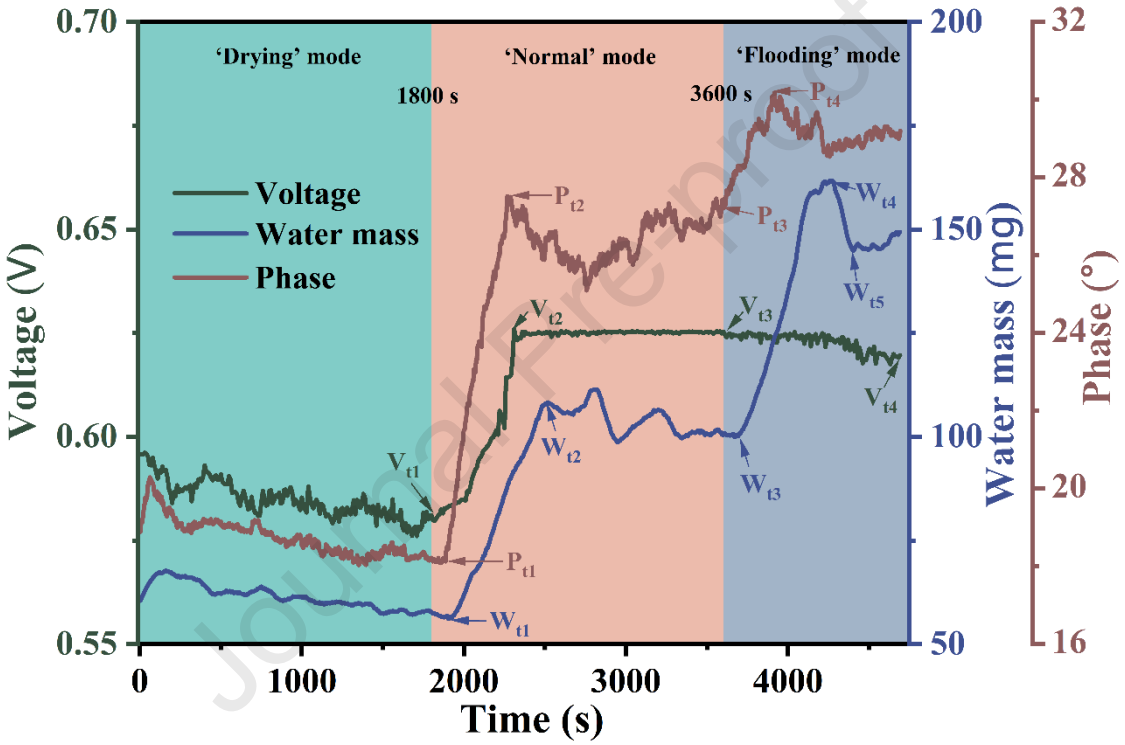

Fig. 11 Evolution of voltage, liquid water mass, and 40 Hz phase angle in a PEFC during galvanostatic operation at 800 mA cm^{-2}.

The results reveal strong correlations between water management and electrochemical performance across three operational regimes: during PEFC operation in Drying mode (0-1800 seconds), the output voltage, 40 Hz impedance phase angle, and liquid water mass collectively exhibited oscillatory declines over time. Although the liquid water mass initially increased during the startup phase (0-180 seconds) due to the electrochemical reaction, it subsequently decreased from a peak of approximately 68 mg to 58 mg. This demonstrates that even at the relatively high current density of 800 mA cm^{-2}, the combined effects of low reactant gas humidity (40% RH at both anode/cathode), elevated operating temperature

(65°C), and high gas flow rates (stoichiometric ratios: cathode 3.5/anode 2.5) progressively deplete internal hydration, inducing membrane drying. It should be noted here that this is of course for a single-cell test set up, and that in a large PEFC stack active hydration is less likely to be critical. The evolution of 40 Hz phase angle closely mirrored liquid water dynamics, rising marginally during initialization before declining from a maximum of 20.3° to 18.1°. Consequently, operation in Drying mode leads to a progressive reduction in the overall liquid water content within the PEFC over time. This dehydration of the membrane decreases proton conductivity [40, 41], which elevates the ohmic resistance and causes a fluctuating decline in output voltage, as observed by the drop from 0.6 V to 0.58 V.

During Normal mode operation (1800-3600 s), the 40 Hz impedance phase angle and liquid water mass exhibited sequential ascending and oscillatory trends, contrasting with the stable terminal voltage profile. Liquid water mass increased rapidly from 58 mg to 108 mg (from 'W_{t1} to W_{t2}'); this phenomenon arises from the combined effects of three operational parameters: elevated reactant gas humidity enhancing water introduction into the PEFC, reduced operating temperature lowering saturation vapor pressure (thereby promoting vapor-to-liquid phase transition), and moderated gas flow rates diminishing water removal capacity. Subsequently, a dynamic equilibrium was established between electrochemical water generation and drainage, yielding sustained oscillations (98-111 mg) before stabilizing at 100 mg. The 40 Hz phase angle mirrored this behavior, rising from 18.1° to 27.5° (from 'P_{t1} to P_{t2}') with subsequent stabilization oscillations (25.1° to 27.5°), demonstrating strong hydration correlation. In contrast, terminal voltage ascended rapidly to 0.63 V (from 'V_{t1} to V_{t2}') and maintained stability, confirming its insensitivity to hydration oscillations under sustained proton conductivity. These diverging trajectories validate normal mode parameter optimization while highlighting the necessity of combined phase angle/water mass monitoring over singular voltage-based hydration assessment.

During Flooding mode operation (3600-4690 seconds), the 40 Hz impedance phase angle and liquid water mass exhibited similar ascending-oscillatory dynamics, contrasting with the monotonic voltage decay. The liquid water mass stabilized transiently at ~100 mg ('W_{t3}') before surging to 162 mg ('W_{t4}'), driven by combined factors: elevated reactant humidity, reduced operating temperature and diminished

gas flow rates. Subsequent partial water expulsion (from 'W_{t4} to W_{t5}') reduced mass to 146 mg, followed by oscillatory recovery to 149 mg through competing electrochemical generation and water removal. The 40 Hz phase angle ascended from 27.2° to 30.2° (from 'P_{t3} to P_{t4}'). Subsequent oscillations emerged, dipping to 28.6° before recovering to 29.2° - indicative of alternating pore-blocking and channel-clearing mechanisms [23]. In contrast, terminal voltage decayed steadily from 0.63 V to 0.62 V (from 'V_{t3} to V_{t4}'), demonstrating delayed sensitivity to mass transport limitations caused by liquid water accumulation in GDLs. This divergence confirms the inadequacy of voltage alone as a diagnostic in detecting initial flooding, where phase angle fluctuations provided advanced warning of critical saturation.

Throughout the full testing period (0-4690 s), a strong correlation ($r = 0.9$) was found between the 40 Hz impedance phase angle and liquid water mass. This positive correlation demonstrates a consistent and closely linked dynamic behavior in these two parameters during the entire operational timeframe, including three different water management modes. Such a strong statistical relationship supports the use of the 40 Hz impedance phase angle as an effective and reliable indicator for tracking changes in hydration state within the PEFC. This indicator can serve as a feedback control parameter for formulating PEFC water management strategies. When the water content of PEFC deviates from the predetermined range, adjustments such as gas humidification or intensified drainage operations can be initiated, thereby enabling the PEFC to achieve long-term stable operation.

Conclusions

Effective water management is essential for the stable and efficient operation of PEFCs, and therefore, rapid and accurate identification of its water content state is crucial. Current diagnostic methods using EIS with the entire frequency range struggle to balance accuracy and real-time capability. This study combines the advantages of EIS measurement and neutron imaging to reveal the relationship between the impedance phase angle at a specific frequency point and the liquid water mass in PEFCs under three operating modes (Normal, Drying, and Flooding). This study presents a rapid and accurate method for identifying the PEFC's hydration state. The key findings can be summarised as follows:

1) Polarization analysis reveals Flooding mode excels at low current densities (0.766 V at 200 mA cm^{-2}) due to enhanced membrane hydration, while Drying mode suffers severe ohmic losses at medium currents (0.685 V at 400 mA cm^{-2}) from dehydration. Normal mode achieves optimal stability and a power density of 589 mW cm^{-2} at 1000 mA cm^{-2}, surpassing the Drying and Flooding modes by 9.5% and 2.1%, respectively.

2) Nyquist plots analysis of EIS data reveals distinct water management mechanisms across operational modes in PEFCs. Drying mode exhibits the highest high frequency resistance (HFR), which is attributed to membrane dehydration impairing proton conductivity. Flooding mode shows significantly elevated low frequency resistance (LFR), which is up to 0.044 Ω cm^2 higher than normal mode at 1000 mA cm^{-2}, indicating severe mass transport limitations from liquid water accumulation in gas diffusion layers. Normal mode demonstrates minimal impedance arcs, reflecting optimal hydration and gas diffusion. Critically, HFR effectively diagnoses drying conditions, while LFR identifies flooding, though LFR measurements face noise challenges and time constraints in dynamic operation.

3) Bode phase analysis identifies the 13-40 Hz frequency band as optimal for differentiating hydration states in PEFCs, where impedance phase angles exhibit maximum discriminability: Flooding mode shows the highest phase angles, while Drying mode shows the lowest. Measurements at 40 Hz (upper limit of this band) reduced perturbation duration from several minutes of the full EIS to only 25 ms per data point, enhancing stability against external interference. Phase angle evolution with current density reveals competing water dynamics: initial reduction (400-600 mA cm^{-2}) stems from accelerated water removal by reactant flow, while subsequent increases (>600 mA cm^{-2}) reflect net accumulation from electrochemical water generation, outweighing drainage. Normal mode maintains balanced hydration until minor flooding resistance at 1000 mA cm^{-2}.

4) Neutron images reveal distinct water distribution patterns: Drying mode shows dispersed droplets in MEA regions; Normal mode exhibits channel-confined clusters with gravity-driven accumulation; Flooding mode demonstrates continuous water columns due to insufficient gas velocity. Liquid water mass decreases at 400-600 mA cm^{-2} but increases beyond 600 mA cm^{-2} in Drying/Flooding modes, while Normal mode maintains efficient drainage.

5) While LFR exhibited significant positive correlations with water mass (r= 0.98) under Drying mode, their correlation coefficient markedly declined in Normal (r= 0.76) and Flooding modes (r= 0.39); conversely, phase angle consistently retains strong positive correlations with water mass ($r \geqslant 0.89$) across all operational regimes, thereby validating its efficacy as a robust hydration-state indicator for PEFCs.

6) During a galvanostatic operation at 800 mA cm^{-2}, phase angle and water mass decline synchronously (e.g., phase angle decreases from 20.3° to 18.1°; water mass decreases from 68 to 58 mg) in Drying mode, while voltage decreases marginally (0.60 to 0.58 V). Normal mode maintains stable voltage despite hydration fluctuations (e.g., water mass oscillates between 98 to 111 mg coupled with phase angle oscillates between 25.1° to 27.5°), underscoring voltage's inadequacy for water-state detection. Phase angle and water mass oscillations during Flooding mode capture dynamic pore-blocking and channel-clearing events, whereas terminal voltage displays response lag to mass transport limitations. Throughout the full testing period (0-4690 s), a strong correlation (r = 0.9) was found between the 40 Hz impedance phase angle and liquid water mass.

Overall, this study proposes a rapid and accurate method for measuring the hydration state of PEFCs by integrating single-frequency impedance phase angle measurement and neutron imaging techniques, demonstrating paramount significance in achieving effective water management in PEFCs. Robust cross-correlation with water content measurements from neutron imaging and multiple testing over different PEFCs in the future could conceivably allow the electrochemical and EIS measurements to become the sole diagnostic for water content, enabling on-board measurements and implementation into a control strategy.

Acknowledgements

Yunsong Wu gratefully acknowledges the financial support from National Natural Science Foundation of China (52307140), Ministry of Education Postdoctoral Overseas Talent Recruitment Special Program, Sichuan Province Postdoctoral Special Grant Program. The authors would also like to acknowledge the financial support from the EPSRC (EP/W03395X/1, EP/X023656/1, EP/W033321/1)

for supporting the Electrochemical Innovation Lab. Jieyang Li thanks the support from the PhD Short-term Visiting Program of Southern University of Science and Technology during his stay at UCL. The authors gratefully acknowledge ISIS for the provision of beam time (https://doi.org/10.5286/ISIS.E.RB2420185).

Appendix A. Supplementary data

Supplementary data to this article can be found online at corresponding position.

References

[1] X. Chen, B. Gu, W. Feng, J. Tan, X. Kong, S. Li, et al., Research on control strategy of PEMFC air supply system for power and efficiency improvement. *Energy*, 2024. 304: 132100.

[2] L. Chen, J. Yang, X. Wu, P. Deng, X. Xu, and Y.J.E. Peng, Remaining useful life prediction of PEMFCs based on mode decomposition and hybrid method under real-world traffic conditions. 2025. 314: 134279.

[3] S. Zhou, J. Dale-Heaps, E. Tavkaya, W. Du, D. Wan, R. Wang, et al., Synchronisation of thermal imaging and multi-channel EIS to interpret planar array PCB fuel cell performance. *Applied Energy*, 2024. 376: 124276.

[4] Y. Xu, Y. Zhang, L. Zhang, R. Fan, Z. Xia, A. Tang, et al., Experimental study of water transport in gas diffusion layer of PEMFC considering the phase-change-induced flow. 2025: 136534.

[5] S. Zhou, L. Xu, P. Trogadas, L. Rasha, W. Du, P.R. Shearing, et al., Effects of an easy-to-implement water management strategy on performance and degradation of polymer electrolyte fuel cells. *Journal of Power Sources*, 2023. 575: 233184.

[6] T. Zhao, W. Fan, H. Cui, M. Liu, T. Zheng, Y. Luan, et al., 3D hybrid-wettability fin channel with dual enhancement of drainage and mass transfer to improve PEMFC performance. *Energy*, 2025. 315: 134378.

[7] S. Zhou, P.R. Shearing, D.J. Brett, and R. Jervis, Machine learning as an online diagnostic tool for proton exchange membrane fuel cells. *Current Opinion in Electrochemistry*, 2022. 31: 100867.

[8] Y. Nie, Z. Sun, and Z.J.E. Chen, Adaptive sliding mode observer for automotive PEMFC membrane water content estimation under hybrid dynamic tests. 2025: 137802.

[9] P. Moçotéguy, B. Ludwig, D. Beretta, and T. Pedersen, Study of the impact of water management on the performance of PEMFC commercial stacks by impedance spectroscopy. *International Journal of Hydrogen Energy*, 2020. 45(33): 16724-16737.

[10] O. Schopen, S. Narayan, M. Beckmann, A.-U.-H. Najmi, T. Esch, and B. Shabani, An EIS approach to quantify the effects of inlet air relative humidity on the performance of proton exchange membrane fuel cells: A pathway to developing a novel fault diagnostic method. *International Journal of Hydrogen Energy*, 2024. 58: 1302-1315.

[11] Z. Liao, K. Li, J. Cao, Y. Gao, C. Yin, and H. Tang. *Early Fault Diagnosis Approach for PEM Stack based on Phase Measurement of Single-Frequency Impedance*. in *IECON 2022–48th Annual Conference of the IEEE Industrial Electronics Society*. 2022. IEEE.

[12] X. Xu, K. Li, Z. Liao, J. Cao, and R. Wang, A Closed-Loop Water Management Methodology for PEM Fuel Cell System Based on Impedance Information Feedback. *Energies*, 2022. 15: 7561.

[13] Q. Li, H. Wang, T. Wang, X. Li, Y. Liu, W. Chen, et al., Online Diagnosis Method of Water Management Faults Based on Hybrid-Frequency Electrochemical Impedance Spectroscopy for PEMFC. *IEEE Transactions on Transportation Electrification*, 2025. 11(1): 2707-2716.

[14] S. Zhou, T. Tranter, T.P. Neville, P.R. Shearing, D.J.L. Brett, and R. Jervis, Fault diagnosis of PEMFC based on the AC voltage response and 1D convolutional neural network. *Cell Reports Physical Science*, 2022. 3: 101052.

[15] J. Chen, M. Perez-Page, C.M. Parlett, Z. Guo, X. Yang, Z. Zhou, et al., Operando synchrotron-based X-ray study and intervention approaches of graphene-related-materials for investigating the performance and durability of HT-PEMFC. *Chemical Engineering Journal*, 2024. 487: 150670.

[16] R.F. Ziesche, J. Hack, L. Rasha, M. Maier, C. Tan, T.M. Heenan, et al., High-speed 4D neutron computed tomography for quantifying water dynamics in polymer electrolyte fuel cells. *Nature Communications*, 2022. 13(1): 1616.

[17] U.U. Ince, H. Markötter, M.G. George, H. Liu, N. Ge, J. Lee, et al., Effects of compression on water distribution in gas diffusion layer materials of PEMFC in a point injection device by means of synchrotron X-ray imaging. *International Journal of Hydrogen Energy*, 2018. 43(1): 391-406.

[18] M. Afra, M. Nazari, M.H. Kayhani, M. Sharifpur, and J. Meyer, 3D experimental visualization of water flooding in proton exchange membrane fuel cells. *Energy*, 2019. 175: 967-977.

[19] Q. Li, K. Sun, M. Suo, Z. Zeng, C. Guan, H. Liu, et al., Water transport in PEMFC with metal foam flow fields: Visualization based on AI image recognition. *Applied Energy*, 2024. 365: 123273.

[20] Y. Wu, Q. Meyer, F. Liu, L. Rasha, J.I.S. Cho, T.P. Neville, et al., Investigation of water generation and accumulation in polymer electrolyte fuel cells using hydro-electrochemical impedance imaging. *Journal of Power Sources*, 2019. 414: 272-277.

[21] P. Boillat, E.H. Lehmann, P. Trtik, and M. Cochet, Neutron imaging of fuel cells – Recent trends and future prospects. *Current Opinion in Electrochemistry*, 2017. 5(1): 3-10.

[22] L. Xu, P. Trogadas, S. Zhou, S. Jiang, Y. Wu, L. Rasha, et al., A Scalable and Robust Water Management Strategy for PEMFCs: Operando Electrothermal Mapping and Neutron Imaging Study. *Advanced Science*, 2024. 11(36): 2404350-2404361.

[23] J.I.S. Cho, T.P. Neville, P. Trogadas, Q. Meyer, Y. Wu, R. Ziesche, et al., Visualization of liquid water in a lung-inspired flow-field based polymer electrolyte membrane fuel cell via neutron radiography. *Energy*, 2019. 170: 14-21.

[24] Y. Wu, L. Xu, S. Zhou, J. Yang, W. Kockelmann, Y. Han, et al., Water management and mass transport of a fractal metal foam flow-field based polymer electrolyte fuel cell using operando neutron imaging. *Applied Energy*, 2024. 364: 123204-123214.

[25] J. Hack, R.F. Ziesche, M. Fransson, T. Suter, L. Helfen, C. Couture, et al., Understanding water dynamics in operating fuel cells by operando neutron tomography: investigation of different flow field designs. *Journal of Physics: Energy*, 2024. 6: 025021.

[26] N. Kulkarni, J.I.S. Cho, L. Rasha, R.E. Owen, Y. Wu, R. Ziesche, et al., Effect of cell compression on the water dynamics of a polymer electrolyte fuel cell using in-plane and through-plane in-operando neutron radiography. *Journal of Power Sources*, 2019. 439

[27] Y. Wu, J.I.S. Cho, X. Lu, L. Rasha, T.P. Neville, J. Millichamp, et al., Effect of compression on the water management of polymer electrolyte fuel cells: An in-operando neutron radiography study. *Journal of Power Sources*, 2019. 412: 597-605.

[28] M.R. Esbo, A.A. Ranjbar, and S.M. Rahgoshay, Analysis of water management in PEM fuel cell stack at dead-end mode using direct visualization. *Renewable Energy*, 2020. 162: 212-221.

[29] A. Iranzo, A. Salva, P. Boillat, J. Biesdorf, E. Tapia, and F. Rosa, Water build-up and evolution during the start-up of a PEMFC: Visualization by means of Neutron Imaging. *International Journal of Hydrogen Energy*, 2017. 42(19): 13839-13849.

[30] M. Nasu, H. Yanai, N. Hirayama, H. Adachi, Y. Kakizawa, Y. Shirase, et al., Neutron imaging of generated water inside polymer electrolyte fuel cell using newly-developed gas diffusion layer with gas flow channels during power generation. *Journal of Power Sources*, 2022. 530: 231251.

[31] J. Kätzel, H. Markötter, T. Arlt, M. Klages, J. Haußmann, M. Messerschmidt, et al., Effect of ageing of gas diffusion layers on the water distribution in flow field channels of polymer electrolyte membrane fuel cells. *Journal of Power Sources*, 2016. 301: 386-391.

[32] S. Zhou, Y. Wu, L. Xu, W. Kockelmann, L. Rasha, W. Du, et al., Water content estimation in polymer electrolyte fuel cells using synchronous electrochemical impedance spectroscopy and neutron imaging. *Cell Reports Physical Science*, 2024. 5: 102208.

[33] J.A. Salva, A. Iranzo, F. Rosa, and E. Tapia, Validation of cell voltage and water content in a PEM (polymer electrolyte membrane) fuel cell model using neutron imaging for different operating conditions. *Energy*, 2016. 101: 100-112.

[34] M.M. Taghiabadi, M. Zhiani, and V.J.A.E. Silva, Effect of MEA activation method on the long-term performance of PEM fuel cell. *Applied Energy*, 2019. 242: 602-611.

[35] T. Minniti, K. Watanabe, G. Burca, D.E. Pooley, and W. Kockelmann, Characterization of the new neutron imaging and materials science facility IMAT. *Nuclear Instruments and Methods in Physics Research Section A: Accelerators, Spectrometers, Detectors and Associated Equipment*, 2018. 888: 184-195.

[36] M. Maier, J. Dodwell, R. Ziesche, C. Tan, T. Heenan, J. Majasan, et al., Mass transport in polymer electrolyte membrane water electrolyser liquid-gas diffusion layers: A combined neutron imaging and X-ray computed tomography study. *Journal of Power Sources*, 2020. 455

[37] Z. Cheng, L. Luo, B. Huang, and Q. Jian, Effect of humidification on distribution and uniformity of reactants and water content in PEMFC. *International Journal of Hydrogen Energy*, 2021. 46(52): 26560-26574.

[38] Y. Yang, H. Jia, Z. Liu, N. Bai, X. Zhang, T. Cao, et al., Overall and local effects of operating parameters on water management and performance of open-cathode PEM fuel cells. *Applied Energy*, 2022. 315: 118978.

[39] Y. Xu, R. Fan, G. Chang, S. Xu, and T. Cai, Investigating temperature-driven water transport in cathode gas diffusion media of PEMFC with a non-isothermal, two-phase model. *Energy Conversion and Management*, 2021. 248: 114791.

[40] T. Miao, C. Tongsh, J. Wang, P. Cheng, J. Liang, Z. Wang, et al., Current density and temperature distribution measurement and homogeneity analysis for a large-area proton exchange membrane fuel cell. *Energy*, 2022. 239: 121922-121933.

[41] V.S. Bethapudi, J. Hack, G. Hinds, P.R. Shearing, D.J.L. Brett, and M.O. Coppens, Electro-thermal mapping of polymer electrolyte membrane fuel cells with a fractal flow-field. *Energy Conversion and Management*, 2021. 250: 114924-114933.

[42] H. Chen, R. Zhang, Z. Xia, Q. Weng, T. Zhang, and P. Pei, Experimental investigation on PEM fuel cell flooding mitigation under heavy loading condition. *Applied Energy*, 2023. 349: 121632.

[43] Y. Wu, J.I.S. Cho, M. Whiteley, L. Rasha, T.P. Neville, R. Ziesche, et al., Characterization of water management in metal foam flow-field based polymer electrolyte fuel cells using in-operando neutron radiography. *International Journal of Hydrogen Energy*, 2020. 45(3): 2195-2205.

[44] J.I.S. Cho, T.P. Neville, P. Trogadas, J. Bailey, P. Shearing, D.J.L. Brett, et al., Capillaries for water management in polymer electrolyte membrane fuel cells. *International Journal of Hydrogen Energy*, 2018. 43(48): 21949-21958.

[45] X. Jia, X. Zhang, L. Xu, Z. Hu, J. Li, and M. Ouyang, Study on relationship between low-frequency impedance and internal states of polymer electrolyte membrane fuel cell based on mass transfer and impedance model. *Journal of Power Sources*, 2024. 592: 233909.

[46] R.F. Ziesche, J. Hack, L. Rasha, M. Maier, C. Tan, T.M.M. Heenan, et al., High-speed 4D neutron computed tomography for quantifying water dynamics in polymer electrolyte fuel cells. *Nat Commun*, 2022. 13(1): 1616-1626.

[47] J. Mitzel, J. Sanchez‐Monreal, D. Garcia‐Sanchez, P. Gazdzicki, M. Schulze, F. Häußler, et al., Fault diagnostics in PEMFC stacks by evaluation of local performance and cell impedance analysis. *Fuel Cells*, 2020. 20(4): 403-412.

[48] P. Moçotéguy, B. Ludwig, D. Beretta, and T. Pedersen, Study of the impact of reactants utilization on the performance of PEMFC commercial stacks by impedance spectroscopy. *International Journal of Hydrogen Energy*, 2021. 46(10): 7475-7488.

[49] Y. Wu, J.I.S. Cho, T.P. Neville, Q. Meyer, R. Ziesche, P. Boillat, et al., Effect of serpentine flow-field design on the water management of polymer electrolyte fuel cells: An in-operando neutron radiography study. *Journal of Power Sources*, 2018. 399: 254-263.

[50] S. Zhou, L. Rasha, L. Xu, W. Du, P.R. Shearing, M.-O. Coppens, et al., Nonuniform compensation of current density distribution in polymer electrolyte fuel cells by local heating. *Energy Conversion and Management*, 2023. 297

[51] X. Wang, Z. Ni, Z. Yang, Y. Wang, and K. Han, Optimization of PEMFC operating parameters considering water management by an integrated method of sensitivity analysis, multi-objective optimization and evaluation. *Energy Conversion and Management*, 2024. 321: 119057.

Highlights

Hydration State Measurement in Polymer Electrolyte Fuel Cells from Correlated Neutron Imaging and Single-Point Impedance

- **A non-invasive method for measuring the hydration state of operating PEFCs.**
- **The single-frequency impedance phase angle integrated with *operando* neutron imaging.**
- **A strong correlation was found between the 40 Hz phase angle and water mass.**

Declaration of interests

☒ The authors declare that they have no known competing financial interests or personal relationships that could have appeared to influence the work reported in this paper.

☐ The authors declare the following financial interests/personal relationships which may be considered as potential competing interests: